



Fabrication of $\text{H}_3\text{PW}_{12}\text{O}_{40}$ -doped carbon nitride nanotubes by one-step hydrothermal treatment strategy and their efficient visible-light photocatalytic activity toward representative aqueous persistent organic pollutants degradation

Kexin Li^a, Liushui Yan^a, Zhenxing Zeng^a, Shenglian Luo^{a,*}, Xubiao Luo^a, Xiaoming Liu^a, Huiqin Guo^a, Yihang Guo^b

^a Key Laboratory of Jiangxi Province for Persistent Pollutants Control and Resources Recycle, Nanchang Hangkong University, Nanchang 330063, PR China

^b School of Chemistry, Northeast Normal University, Changchun 130024, PR China

ARTICLE INFO

Article history:

Received 10 December 2013

Received in revised form 3 March 2014

Accepted 9 March 2014

Available online 19 March 2014

Keywords:

Graphitic carbon nitride

Polyoxometalate

Nanotubes

Hydrothermal treatment

Persistent organic pollutants

ABSTRACT

A series of $\text{H}_3\text{PW}_{12}\text{O}_{40}$ -doped carbon nitride nanotubes ($\text{H}_3\text{PW}_{12}\text{O}_{40}/\text{C}_3\text{N}_4$ NTs) are prepared using one-step hydrothermal treatment, with $\text{g-C}_3\text{N}_4$ and $\text{H}_3\text{PW}_{12}\text{O}_{40}$ as precursors. The morphology, porosity, phase, chemical structure, and optical and electronic properties of $\text{H}_3\text{PW}_{12}\text{O}_{40}/\text{C}_3\text{N}_4$ NTs are characterized. Subsequently, the photocatalytic activity of $\text{H}_3\text{PW}_{12}\text{O}_{40}/\text{C}_3\text{N}_4$ NTs is evaluated through the degradation of representative aqueous persistent organic pollutants methyl orange and diethyl phthalate under visible-light ($\lambda > 420$ nm) irradiation. The photocatalytic activity of $\text{H}_3\text{PW}_{12}\text{O}_{40}/\text{C}_3\text{N}_4$ NTs is significantly enhanced compared with $\text{g-C}_3\text{N}_4$ as a result of its unique tubular nanostructure, enhanced quantum efficiency, and high light utilization efficiency. Finally, the reusability of $\text{H}_3\text{PW}_{12}\text{O}_{40}/\text{C}_3\text{N}_4$ NTs is evaluated under four consecutive photocatalytic runs.

© 2014 Elsevier B.V. All rights reserved.

1. Introduction

Using direct visible-light in the degradation of aqueous persistent organic pollutants (POPs) is a research focus in the field of environmental science [1–3]. Graphitic carbon nitride ($\text{g-C}_3\text{N}_4$) has been widely developed as an effective organic semiconductor photocatalyst for aqueous POPs degradation since its visible-light photocatalytic activity in hydrogen production was discovered by Wang's group [4–7]. The $\text{g-C}_3\text{N}_4$ possesses more practical application value than conventional TiO_2 photocatalysts because of its stable chemical structure, narrow band gap (2.7 eV), and low preparation cost. However, $\text{g-C}_3\text{N}_4$ has disadvantages as a metal-free photocatalyst, such as its bulk layered structure, rapid photogenerated electron–hole (e^- – h^+) pair recombination and low visible-light utilization efficiency; therefore, the visible-light activity of $\text{g-C}_3\text{N}_4$ is low in practical applications [8–10]. Nanostructural $\text{g-C}_3\text{N}_4$ design and development of $\text{g-C}_3\text{N}_4$ -based heterostructured photocatalysts are two main strategies to improve the visible-light

photocatalytic activity of $\text{g-C}_3\text{N}_4$. Yang et al. fabricated $\text{g-C}_3\text{N}_4$ nanosheets using a liquid-exfoliation method to enhance the hydrogen evolution activity of $\text{g-C}_3\text{N}_4$ under visible light irradiation, and Du et al. developed a hybrid graphene and $\text{g-C}_3\text{N}_4$ nanocomposite to improve the visible light response of $\text{g-C}_3\text{N}_4$ [11,12].

Tubular nanomaterials, such as titania nanotubes, have elicited much attention in photocatalysis fields because of their unique physicochemical properties and photocatalytic performances [13,14]. A tubular nanostructure can provide internal and external surface active sites for photocatalytic reactions, facilitate photo-generated electron transfer, and reduce mass transfer resistance of photocatalytic reactions [15,16]. Therefore, carbon nitride nanotubes (C_3N_4 NTs) design is very significant in improving $\text{g-C}_3\text{N}_4$ photocatalytic activity and C_3N_4 NTs-based hybrid material development. Some groups have attempted to prepare C_3N_4 NTs using catalytic self-assembly, template, and chemical vapor deposition methods [17–19]. However, these methods are limited by harsh reaction conditions, operational complexity, toxicity, and high cost. Hydrothermal treatment is an effective “green” synthetic process of preparing C_3N_4 NTs using $\text{g-C}_3\text{N}_4$ directly through a distinctive nanosheet roll-up mechanism and does not require a

* Corresponding author. Tel.: +86 791 83953373; fax: +86 791 83953373.
E-mail address: sllou@hnu.edu.cn (S. Luo).

structure-directing agent [20,21]. Several groups have reported on the hydrothermal synthesis of titania NTs [22]. However, preparation of C_3N_4 NTs using hydrothermal synthesis method has not been reported thus far.

Constructing $g-C_3N_4$ -based hybrid materials, such as $Ag/g-C_3N_4$, $Pt/g-C_3N_4$ and $CdS/g-C_3N_4$, is an efficient method to improve the visible-light activity of $g-C_3N_4$ by reducing e^- - h^+ pair recombination and/or enhancing visible-light utilization efficiency [23–25]. However, hybrid photocatalyst exploration is primarily limited by cost and environment friendliness. 12-Tungstophosphoric acid ($H_3PW_{12}O_{40}$) is a widely used polyoxometalate in homogeneous photocatalytic reactions and is an efficient electron trap with a well-defined Keggin structure [26,27]. Therefore, doping $H_3PW_{12}O_{40}$ in semiconductor photocatalysts is an effective method to reduce e^- - h^+ pair recombination. $H_3PW_{12}O_{40}$ exhibits more advantages in actual application compared with noble metals and CdS precursors because of its low cost and lack of toxicity. Our previous work has proven that the combination of $H_3PW_{12}O_{40}$ and TiO_2 can enhance the photocatalytic efficiency of TiO_2 -catalyzed reactions as a result of the strong electron acceptability in $H_3PW_{12}O_{40}$ and electron transfer from $H_3PW_{12}O_{40}$ to oxygen species in the reaction medium [28,29]. The Keggin unit has a synergistic photocatalytic effect on the TiO_2 matrix and retards photogenerated e^- - h^+ pair recombination because photogenerated electrons are trapped in the unoccupied W 5d states of the Keggin unit.

A series of $H_3PW_{12}O_{40}/C_3N_4$ NTs are prepared through one-step hydrothermal treatment using $H_3PW_{12}O_{40}$ and $g-C_3N_4$ as precursors in this study. The as-prepared $H_3PW_{12}O_{40}/C_3N_4$ NTs are expected to exhibit higher visible-light photocatalytic activity than $g-C_3N_4$ given their unique tubular nanostructure and the strong electron acceptability of the Keggin unit. The morphology, porosity, phase, chemical structure, and optical and electronic properties of $H_3PW_{12}O_{40}/C_3N_4$ NTs are characterized. The photocatalytic activity of $H_3PW_{12}O_{40}/C_3N_4$ NTs is evaluated by the degradation and mineralization of representative aqueous POPs methyl orange (MO) and diethyl phthalate (DEP) under visible-light irradiation ($\lambda > 420$ nm). MO is an organic dye that is typically used to test the catalytic activity of a photocatalyst. DEP is an endocrine-disrupting chemical that is widely applied industrially, agriculturally, and domestically, especially as a plasticizer [30–32]. The release of DEP into either the ecosystem or wastewater effluent has resulted in numerous human diseases and pollutants [33,34]. Thus, the selection of DEP as a target pollutant to study the visible-light photocatalytic activity of as-prepared hybrid materials is significant. DEP is also a stable compound in the natural environment as a result of the existence of the benzene carboxylic group and the lack of light response at wavelengths longer than 300 nm. DEP degradation as a consequence of sensitization effect can be excluded in the current photocatalytic system, unlike dyes that have a visible-light response.

2. Experimental

2.1. Chemicals and reagents

Melamine ($C_3H_6N_6$, AR grade, $MW = 126.12 \text{ g mol}^{-1}$) was purchased from Tianjin Damao Chemical Reagent. 12-Tungstophosphoric acid ($H_3PW_{12}O_{40}$, AR grade, $MW = 2880.05 \text{ g mol}^{-1}$) and diethyl phthalate ($C_{12}H_{14}O_4$, GC grade, $MW = 222.24 \text{ g mol}^{-1}$) were purchased from Aladdin Chemistry Co. Ltd. Methyl orange ($C_{14}H_{14}N_3NaO_3S$, AR grade, $MW = 327.33 \text{ g mol}^{-1}$) was purchased from Shanghai Fine Chemical Technology Co. Ltd. All chemicals were used without further purification. Double distilled water was used in the catalyst preparation and subsequent catalytic tests.

2.2. Catalyst preparation

2.2.1. Preparation of $g-C_3N_4$

Pure $g-C_3N_4$ sample was prepared by directly calcining melamine in air. Typically, 50 g of melamine powder was put into a 100 mL alumina crucible with a cover. The crucible was heated to 250°C from room temperature in a muffle furnace at a heating rate of 5°C/min , and then continued heated to 550°C at a heating rate of 10°C/min . Keeping the temperature at 550°C for 2 h, the yellow $g-C_3N_4$ sample was obtained after natural cooling.

2.2.2. Preparation of $H_3PW_{12}O_{40}/C_3N_4$ NTs hybrid materials

The $g-C_3N_4$ nanosheets suspension was obtained by peeling off 1 g of bulk $g-C_3N_4$ powder in 15 mL water using a 500 W ultrasonic crusher for 1 h at room temperature. The desired amount of $H_3PW_{12}O_{40}$ (0.1, 0.3, 0.5, and 0.7 g) was dissolved in 15 mL HCl (2 mol L^{-1}). The above $H_3PW_{12}O_{40}/\text{HCl}$ solution was successively added into the $g-C_3N_4$ nanosheets suspension. After stirring the resulting mixture for 1 h at room temperature, the mixture was subject to hydrothermal treatment at 150°C for 24 h at a heat rate of 1°C/min . The final products were obtained by drying at 60°C for 24 h and thermal treatment at 120°C for 24 h, respectively. The product was denoted as $H_3PW_{12}O_{40}/C_3N_4$ NTs (x:y), where x:y represents the mass ration of $H_3PW_{12}O_{40}$ to $g-C_3N_4$. For comparison, C_3N_4 NTs and $H_3PW_{12}O_{40}/\text{MCM-41}$ (3:10) samples were also prepared by the same method but in the absence of $H_3PW_{12}O_{40}$ precursor and use MCM-41 as a support.

2.3. Catalyst characterizations

Transmission electron microscopy (TEM) images were recorded on a JEOL JEM-2010 transmission electron microscope at an accelerating voltage of 200 kV. Field emission scanning electron microscopy (FESEM) images were recorded using a JEOL JSM-6700 F field emission scanning electron microscope. The chemical compositions and elemental mappings of the samples were determined by energy-dispersive X-ray spectrometer (EDX) equipped on TEM and FESEM. Nitrogen gas porosimetry measurements were performed on a Quantachrome NOVA 2000e surface area and porosity analyzer after the samples were outgassed under a vacuum at 70°C for 20 min and 150°C for 6 h. X-ray diffraction (XRD) patterns were obtained using a Panalytical X'Pert PRO diffractometer via $\text{Cu K}\alpha$ radiation. Fourier transform infrared (FTIR) spectra were recorded on a Bruker VERTEX 70 FTIR apparatus. X-ray photoelectron spectra (XPS) was performed using a VG-ADES 400 instrument with an $\text{Mg K}\alpha$ -ADES source at a residual gas pressure of less than 10^{-8} Pa. UV–visible/diffuse reflectance spectroscopy (UV–vis/DRS) was conducted using a Lambda 750 S UV/VIS/NIR spectrometer. Photoluminescence (PL) measurements were carried out on a HITACHI F-7000 fluorescence spectrophotometer.

2.4. Photocatalytic tests

A PLS-SXE300 Xe lamp (Beijing PerfectLight Co. Ltd., China) served as the simulated sunlight source, and the output wavelength $\lambda > 320$ nm. The visible light irradiation was obtained by removing the UV irradiation from the lamp using a 420 nm cut filter, which can control the output wavelength $\lambda > 420$ nm. The suspension containing 200 mg of solid catalyst and 100 mL of aqueous POPs solution was poured into a 300 mL self-designed quartz reactor. The initial concentration of aqueous POPs is 10 mg L^{-1} . The suspension was ultrasonicated for 10 min and stirred in the dark until adsorption–desorption equilibrium. Subsequently, the light source was switched on, and further stirring was applied. At specific intervals of irradiation, fixed amounts of the reaction solution were extracted, centrifuged, and filtered. Changes in the

MO concentrations were analyzed using an UNICO UV-2000 spectrophotometer at $\lambda = 464$. Changes in the DEP concentrations were analyzed using an Agilent 1100 series high-performance liquid chromatography (HPLC): C₁₈ column, UV detector ($\lambda = 227$ nm), and acetonitrile/water (60/40, v/v) was used as a mobile phase at a flow rate of 1.0 mL/min. Changes of total organic carbon (TOC) in the reaction system were monitored using a Shimadzu TOC-L CSH total organic carbon analysis system. The intermediate products in aqueous solution were identified by Agilent 1100 series high-performance liquid chromatography/mass spectrometry detector (HPLC/MSD Trap/VL).

2.5. Photocurrent measurements

Photocurrent measurements were carried out using the conventional three electrode setup connected to an electrochemical station (CHI 630E, Shanghai Chenhua, China). In this electrochemical system, the prepared catalyst/Ti sheet was used as the working electrode; a Pt wire was used as the counter electrode and an Ag/AgCl electrode (saturated KCl) was used as the reference electrode. The electrolyte was 0.01 mol L⁻¹ Na₂SO₄ aqueous solution (100 mL). A 300 W Xe lamp served as a light source. The measurements were carried out at a constant potential of +1.0 V to the working electrode.

3. Results and discussion

3.1. Fabrication of H₃PW₁₂O₄₀/C₃N₄ NTs by one-step hydrothermal treatment

The efficient immobilization of a functional component within a solid semiconductor photocatalyst is fundamentally important in the design of hybrid photocatalyst for photocatalytic reactions. Photocatalytic activity and stability during reactions are important attributes for a useful photocatalyst. Thus, hydrothermal treatment is a powerful tool. The following two factors should be considered in the preparation and design of H₃PW₁₂O₄₀/C₃N₄ NTs. First, the hybridization of C₃N₄ NTs and Keggin units should not affect the primary Keggin structure. H₃PW₁₂O₄₀ begins to decompose at temperatures higher than 465 °C [35]; therefore, the preparation of H₃PW₁₂O₄₀/C₃N₄ NTs should be performed under relatively low temperatures. Second, the interaction between C₃N₄ NTs and Keggin units should be strong to minimize H₃PW₁₂O₄₀ loss during the photocatalytic reaction process. Hydrothermal treatment can ensure this strong interaction because various chemical bonds are formed during the hydrothermal process.

The characterization results proved that H₃PW₁₂O₄₀/C₃N₄ NTs were successfully prepared using one-step hydrothermal treatment. The mixture of g-C₃N₄ and water at room temperature underwent ultrasonic crashing, and the bulk layered g-C₃N₄ was peeled off to form g-C₃N₄ nanosheets. Subsequently, the H₃PW₁₂O₄₀/HCl solution was added successively to the g-C₃N₄ nanosheets suspension at room temperature. H₃PW₁₂O₄₀ and g-C₃N₄ nanosheets reached adsorption–desorption equilibrium after 1 h continuous stirring. HCl was added to the current preparation system as a Keggin unit structural protective agent and a hydroxyl condensation reaction catalyst during hydrothermal treatment. The H₃PW₁₂O₄₀ and g-C₃N₄ nanosheets mixture was subjected to hydrothermal treatment at 150 °C for 24 h. The surface –NH₂ groups within g-C₃N₄ nanosheets were substituted with the –OH groups during hydrothermal treatment, and the g-C₃N₄ nanosheets were curled and scrolled to C₃N₄ NTs due to the condensation of surface –OH groups. The proposed tubular nanostructure reduced the charge imbalance caused by unsaturated or dangling bonds at the edges of the intermediate structure [36]. Other authors have

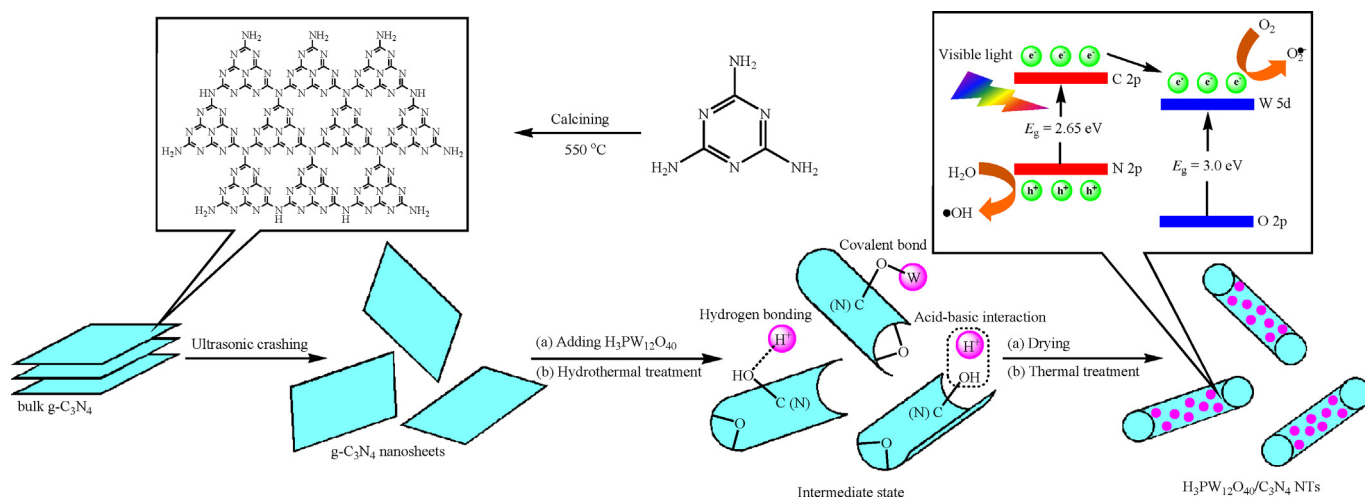
justified nanotubes formation through an asymmetric chemical environment or mechanical stress [37,38]. We propose that tubular nanostructure formation originate from the condensation of unbonded surface –OH groups during hydrothermal treatment. The H⁺ originated from HCl and/or H₃PW₁₂O₄₀ in the current preparation system perform as a –OH condensation reaction catalyst. Keggin units link to C₃N₄ NTs through the formed covalent W–O–C bonds because of the interactions between either terminal W=O bonds or bridge W–O–W bonds within Keggin units and the surface –OH groups within the C₃N₄ NTs. Hydrogen bonding and acid–base interactions between the oxygen atoms of the Keggin anion and the surface –OH groups in C₃N₄ NTs may also exist in the hybrid materials. Similar results have been reported in our previous work [29]. The interaction between H₃PW₁₂O₄₀ and C₃N₄ NTs was reinforced after thermal treatment at 120 °C for 24 h. The preparation route and constructed wall component based on the discussion above is shown in Scheme 1.

3.2. Characterization

3.2.1. Morphology and textural property

The morphologies of bulk g-C₃N₄, C₃N₄ NTs, and H₃PW₁₂O₄₀/C₃N₄ NTs (represented by H₃PW₁₂O₄₀/C₃N₄ NTs (1:10) and H₃PW₁₂O₄₀/C₃N₄ NTs (3:10)) are revealed by TEM observations presented in Fig. 1. Bulk g-C₃N₄ exhibits a graphite-like layered structure with more than five layers (Fig. 1a). The opened ends of the C₃N₄ NTs array clearly reveal a hollow, tubular structure, as shown in Fig. 1b. The outer diameter of these C₃N₄ NTs is approximately 100 nm, and the wall thickness is approximately 10 nm. The above TEM results indicate that C₃N₄ NTs are successfully prepared through hydrothermal treatment using bulk g-C₃N₄ as a direct precursor. The black H₃PW₁₂O₄₀ clusters adhere to the inner and outer surfaces of C₃N₄ NTs after H₃PW₁₂O₄₀/C₃N₄ NTs formation. This finding indicates the formation of interfacial interaction between H₃PW₁₂O₄₀ and C₃N₄ NTs (Fig. 1c and d). Irregular pore structures notably appear on the walls of the H₃PW₁₂O₄₀/C₃N₄ NTs. Pore size increases when the amount of H₃PW₁₂O₄₀ added in the initial catalyst preparation process is increased because of the impact damage inflicted by large H₃PW₁₂O₄₀ clusters under high temperature and pressure conditions. The tubular nanostructure and wall nanopores are more advantageous compared with the bulk layered structure of g-C₃N₄ in the reduction of mass transfer resistance of photocatalytic reactions. EDX spectrum and corresponding EDX elemental mappings results from selected area show that the C, N, O, and W elements exist in the hybrid materials and W element homogeneously distribute throughout the whole nanotubes (Fig. 1e–g). The homogeneously distributed W element proves the uniform distribution of H₃PW₁₂O₄₀ in the H₃PW₁₂O₄₀/C₃N₄ NTs.

The morphological evolution from bulk layered structure into nanotube can be confirmed by FESEM observation, as presented in Fig. 2a–d. The bulk layered structure of g-C₃N₄ can be observed in Fig. 2a, which is consistent with the TEM observation. As expected, the bulk g-C₃N₄ is successfully exfoliated to form g-C₃N₄ nanosheets after ultrasonic crashing (Fig. 2b). Both a half-rolled up nanosheet and a completed nanotube are shown in the FESEM images of H₃PW₁₂O₄₀/C₃N₄ NTs (3:10) (Fig. 2c and d). This finding indicates that the tubular nanostructure was constructed by curling g-C₃N₄ nanosheets during the hydrothermal treatment. For the H₃PW₁₂O₄₀/C₃N₄ NTs (3:10), the W elemental mappings show that H₃PW₁₂O₄₀ homogeneously distribute on the both half-rolled up nanosheet and completed nanotube (Fig. S1). Therefore, it can be inferred that the H₃PW₁₂O₄₀ clusters should distribute both the inner and the outer surfaces of C₃N₄ NTs. The above TEM and FESEM results of H₃PW₁₂O₄₀/C₃N₄ NTs indicate that there is no adverse



Scheme 1. The designed route for fabrication of $\text{H}_3\text{PW}_{12}\text{O}_{40}/\text{C}_3\text{N}_4$ NTs and the separation and transportation of photoinduced charge carriers in the $\text{H}_3\text{PW}_{12}\text{O}_{40}/\text{C}_3\text{N}_4$ system under visible-light irradiation.

impact of Keggin anion on the rolling $\text{g-C}_3\text{N}_4$ nanosheets to form C_3N_4 NTs.

The textural property of bulk $\text{g-C}_3\text{N}_4$, C_3N_4 NTs, and $\text{H}_3\text{PW}_{12}\text{O}_{40}/\text{C}_3\text{N}_4$ NTs is characterized by nitrogen gas porosity measurement. The obtained sorption isotherms and BJH (Barrett–Joyner–Halenda) pore-size distribution curves are shown in Fig. 3. All of the tested materials exhibit type IV isotherms with H3 hysteresis loops regardless of morphology and amount of $\text{H}_3\text{PW}_{12}\text{O}_{40}$ added, thus indicating the mesoporosity of the materials (Fig. 3a). The BET (Brunauer–Emmett–Teller) surface areas of C_3N_4 NTs are twice enlarged compared with that of bulk $\text{g-C}_3\text{N}_4$, mainly because both external and internal geometrical surfaces are exposed. The BET surface areas gradually decrease when the mass ratio of $\text{H}_3\text{PW}_{12}\text{O}_{40}$ to $\text{g-C}_3\text{N}_4$ increases from 1:10 to 5:10. This result suggests that the C_3N_4 NTs are partially blocked after a large amount of Keggin units is introduced. The pore-size distribution curve of bulk $\text{g-C}_3\text{N}_4$ exhibits a mesopore centered at 4.1 nm, as shown in Fig. 3b. The presence of this mesopore is attributed to

the released NH_3 , which act as soft templates during melamine polymerization [39]. Other broad pore-size distribution peaks centered at 5.6, 6.8, 5.8, and 6.7 nm can be observed in C_3N_4 NTs and $\text{H}_3\text{PW}_{12}\text{O}_{40}/\text{C}_3\text{N}_4$ NTs samples, with the exception of that centered at 4.1 nm. These mesopores originated from the mesostructure on the wall and at the open nanotube end. This finding agrees with the TEM and FESEM observations. The $\text{H}_3\text{PW}_{12}\text{O}_{40}/\text{C}_3\text{N}_4$ NTs pore-size distribution peaks centered at 4.1 nm weakened, possibly because of the filling effect of small $\text{H}_3\text{PW}_{12}\text{O}_{40}$ clusters.

3.2.2. Compositional and structural information

The composition and structure of bulk $\text{g-C}_3\text{N}_4$, C_3N_4 NTs, and $\text{H}_3\text{PW}_{12}\text{O}_{40}/\text{C}_3\text{N}_4$ NTs are measured by XRD, FTIR spectroscopy, and XPS. The phase structures of bulk $\text{g-C}_3\text{N}_4$, C_3N_4 NTs, and $\text{H}_3\text{PW}_{12}\text{O}_{40}/\text{C}_3\text{N}_4$ NTs are analyzed by XRD (Fig. 4). For the bulk $\text{g-C}_3\text{N}_4$ sample, the strong (002) peak at 27.4° corresponds to an interlayer distance of $d = 0.33 \text{ nm}$, whereas the (100) peak at 12.8° represents in-plane structural packing motif with a period

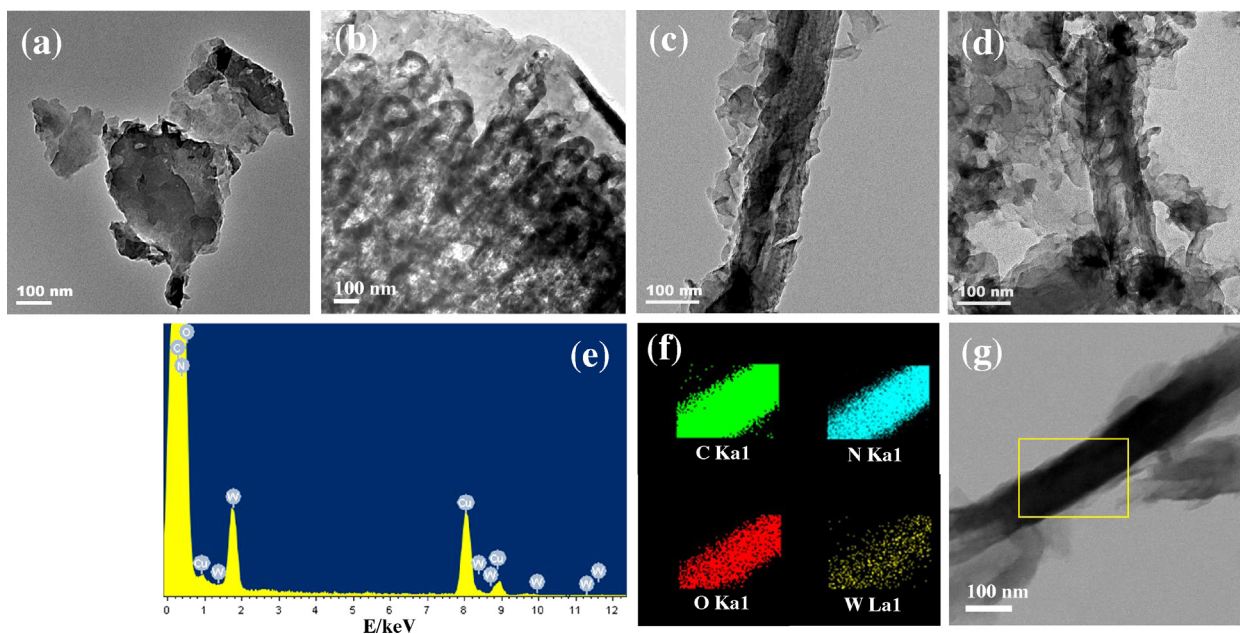


Fig. 1. TEM images of bulk $\text{g-C}_3\text{N}_4$ (a), C_3N_4 NTs (b), $\text{H}_3\text{PW}_{12}\text{O}_{40}/\text{C}_3\text{N}_4$ NTs (1:10) (c), and $\text{H}_3\text{PW}_{12}\text{O}_{40}/\text{C}_3\text{N}_4$ NTs (3:10) (d). EDX spectrum (e) and corresponding EDX elemental mappings (f) of $\text{H}_3\text{PW}_{12}\text{O}_{40}/\text{C}_3\text{N}_4$ NTs (3:10) from selected area (g) for C, N, O, and W regions.

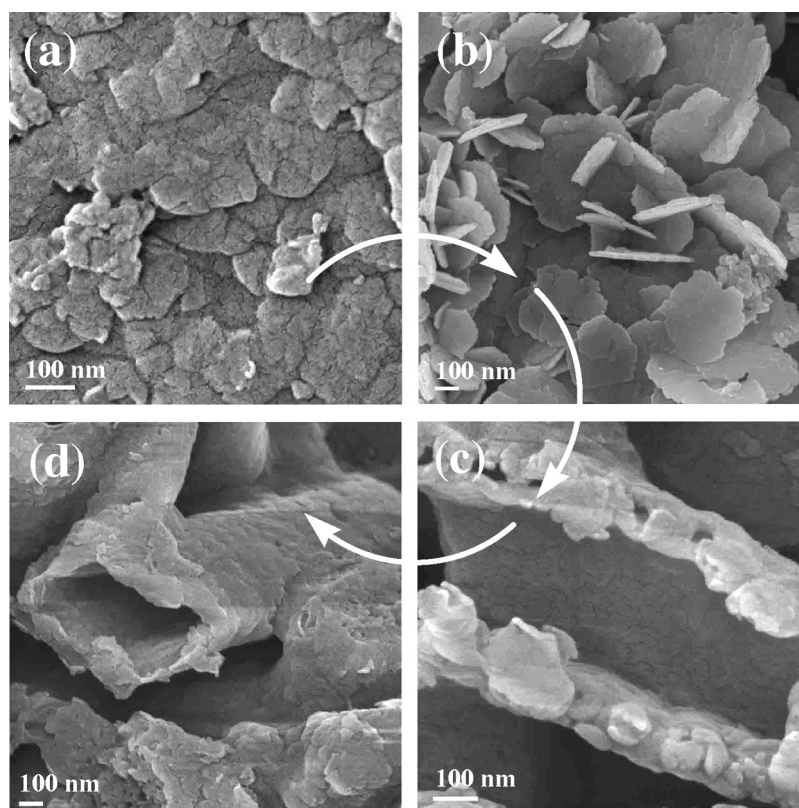


Fig. 2. FESEM images of the morphological evolution from bulk layered structure into nanotube: bulk g-C₃N₄ (a), g-C₃N₄ nanosheets (b), a half-rolled up nanosheet (c), and a completed nanotube (d).

of 0.675 nm [40]. As for the C₃N₄ NTs, the intensity of the (002) peak significantly decreases and the (100) peak disappears completely, indicating that the layered structure units of bulk g-C₃N₄ has reduced and transformed morphologically into a tubular nanostructure after ultrasonic crashing and hydrothermal treatment. The intensity of the H₃PW₁₂O₄₀/C₃N₄ NTs peak at 27.4° gradually weakens, and the intensity of the H₃PW₁₂O₄₀-related peak at 26.4° gradually increases when the mass ratio of H₃PW₁₂O₄₀ to g-C₃N₄ increases from 1:10 to 5:10. This result is attributed to the effect of composition variation in similar hybrid materials on relative diffraction intensity.

Fig. 5 shows the FTIR spectra of bulk g-C₃N₄, H₃PW₁₂O₄₀ precursor, C₃N₄ NTs, and H₃PW₁₂O₄₀/C₃N₄ NTs. For the bulk g-C₃N₄ sample, a series of peaks are located in the range 1700–1000 cm^{−1}, as shown in Fig. 5a. This result is attributed to stretching modes, such as C–N and C=N in the CN heterocycles. The sharp peak at 806.7 cm^{−1} denotes the typical bending vibration of s-triazine units. The broad absorption peaks located at 3400 cm^{−1} to 2800 cm^{−1} originate from the stretching vibrational modes of primary (–NH₂) and secondary (=NH) amines, which are associated with uncondensed amino groups [41]. The FTIR spectrum of C₃N₄ NTs is clearly similar to that of bulk g-C₃N₄, indicating that C₃N₄ NTs undergoing hydrothermal treatment maintain a chemical structure similar to that of bulk g-C₃N₄. C₃N₄ NTs notably display a stronger FTIR mode than bulk g-C₃N₄ because they have more exposed surface functional groups. As shown in Fig. 5b, characteristic H₃PW₁₂O₄₀ frequencies related to the Keggin unit are 1075, 975, 895, and 762 cm^{−1}, respectively. These frequencies are attributed to vibrations in the P–O_a bonds of the PO₄ units, W=O_d bonds, and two W–O_{b/c}–W bonds of the Keggin unit [42]. H₃PW₁₂O₄₀-related FTIR modes change to 1072, 972, 900, and 755 cm^{−1} after H₃PW₁₂O₄₀/C₃N₄ NTs formation when the mass ratio of H₃PW₁₂O₄₀ to g-C₃N₄ increases from 1:10 to

5:10. This result implies that the primary Keggin structure remains intact after being introduced into the C₃N₄ NTs using the current hydrothermal treatment strategy. Moreover, the interfaces of the Keggin unit and C₃N₄ NTs strongly interact. C₃N₄ NTs-related FTIR modes cannot be observed in the FTIR spectra of H₃PW₁₂O₄₀/C₃N₄ NTs because the strong FTIR modes of the Keggin unit covers them.

Existing interactions between Keggin unit and C₃N₄ NTs can be further confirmed by high-resolution XPS analysis (Fig. 6). As shown in Fig. 6a, the C 1s peak centered at 284.6 eV is typically assigned to C–C or/and C=C, which originates from the adventitious reference carbon on the surface [43]. For the bulk g-C₃N₄ sample, the C 1s peak centered at 287.8 eV originates from sp² C atoms bonded to N in an aromatic ring (N=C(N)₂), whereas the C 1s peak centered at 288.6 eV is assigned to sp² C atoms in the aromatic ring attached to the primary and secondary amines (N=C(N)–NH, N=C(N)–NH₂). The C 1s peaks of C₃N₄ NTs that originate from sp² C atoms shift to a higher banding energy direction after suffer from hydrothermal treatment, indicating that the –NH₂ groups within bulk g-C₃N₄ has been substituted with the –OH groups to form an N=C(N)–OH species. The original electronic environment of sp² C atoms is perturbed by the –OH groups. As for the two H₃PW₁₂O₄₀/C₃N₄ NTs samples, the shift of C 1s peaks, which originate from sp² C atoms, becomes evident because of the strong electronic pull of the Keggin unit. The result implies that either terminal W=O or bridge W–O–W groups within Keggin units interact with the N=C(N)–OH species within C₃N₄ NTs via covalent C–O–W bonds. The results of N 1s binding energy region can support the high-resolution XPS analysis of C 1s described above (Fig. 6b). For the bulk g-C₃N₄ sample, the peak centered at 398.3 eV is assigned to sp² hybridized aromatic nitrogen atoms bonded to carbon atoms (C–N=C). The peak centered at 399.1 eV is related to either tertiary nitrogen N–(C)₃ groups linking structural motif

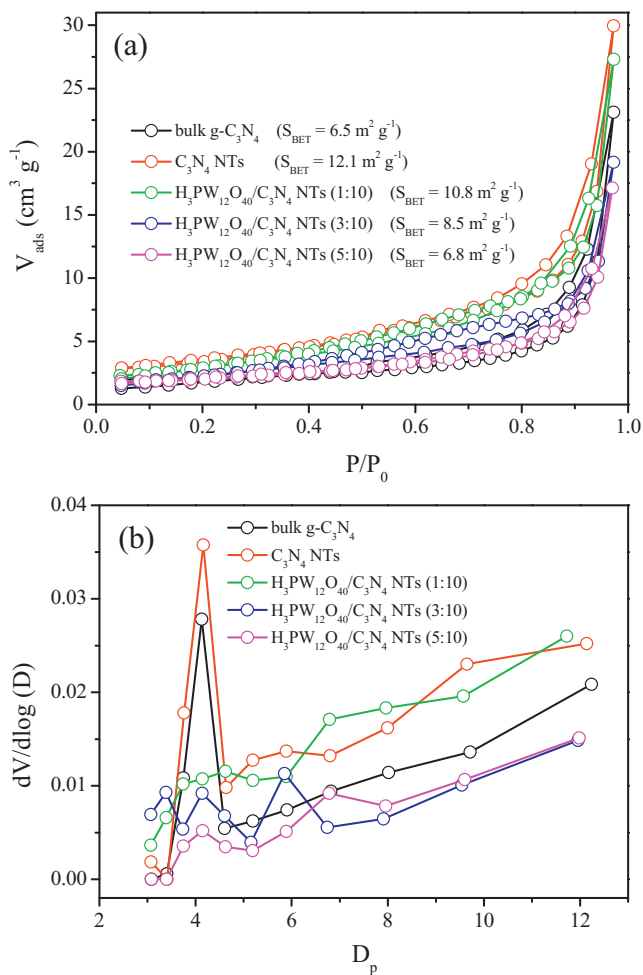


Fig. 3. Nitrogen gas adsorption-desorption isotherms (a) and BJH pore-size distribution curves (b) of bulk g-C₃N₄, C₃N₄ NTs, and H₃PW₁₂O₄₀/C₃N₄ NTs.

(C₆N₇) or amino groups carrying hydrogen (HN-(C)₂, H₂N-C) to structural defects and incomplete condensation. A weak peak centered at 401.2 eV corresponds to nitrogen atoms bonded to three carbon atoms in the aromatic cycles [44]. As for the C₃N₄ NTs and two H₃PW₁₂O₄₀/C₃N₄ NTs samples, the peak centered at 399.1 eV becomes weak because of the missing -NH₂ group, and the shift of N 1s peaks is attributed to -OH groups substitution

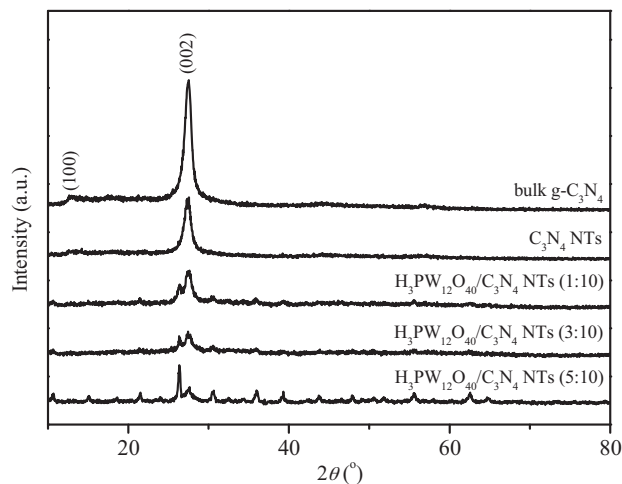


Fig. 4. XRD patterns of bulk g-C₃N₄, C₃N₄ NTs, and H₃PW₁₂O₄₀/C₃N₄ NTs.

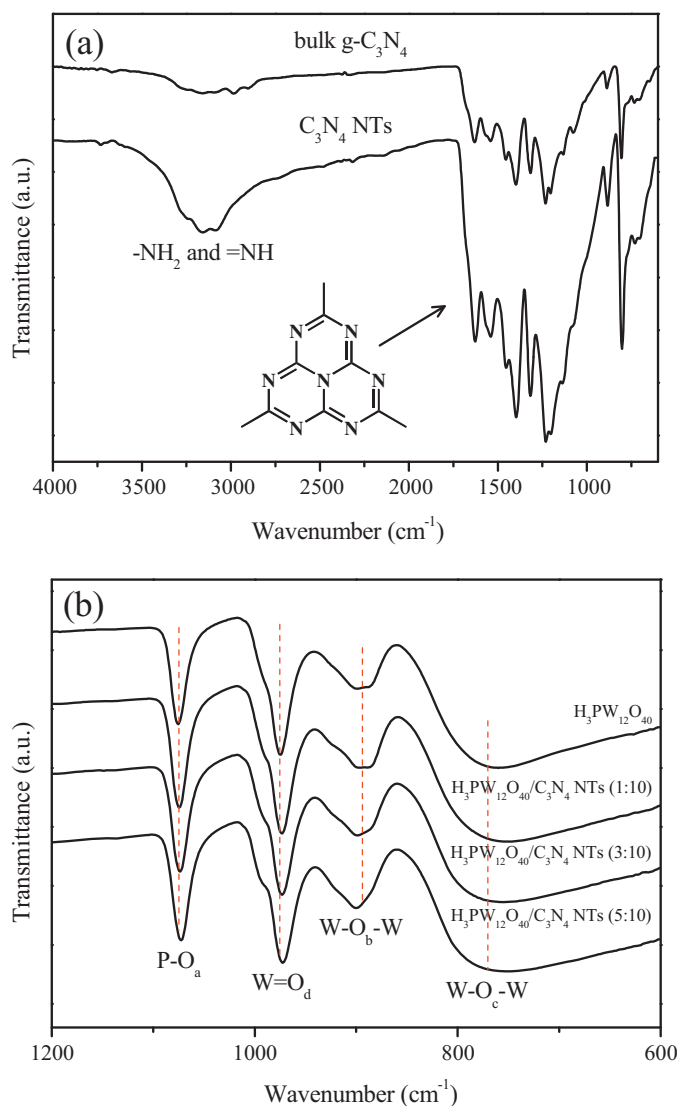


Fig. 5. FTIR spectra of bulk g-C₃N₄, C₃N₄ NTs, H₃PW₁₂O₄₀ precursor, and H₃PW₁₂O₄₀/C₃N₄ NTs.

and covalent C-O-W bonds formation. As shown in Fig. 6c, bulk g-C₃N₄ shows only one O 1s peak centered at 532.8 eV, ascribed to the adsorbed water. After suffer from hydrothermal treatment, the other O 1s peak centered at 532.1 eV is detected on the C₃N₄ NTs sample. This signal is attributed to the formation of N=C(N)-OH species. Pure H₃PW₁₂O₄₀ sample shows three O 1s peaks centered at 530.7, 532.7, and 533.3 eV, which is assigned to W-O-W, W-O-P/W-O-H, and adsorbed water, respectively. As for the two H₃PW₁₂O₄₀/C₃N₄ NTs samples, the broad O 1s peaks originate from the binding energy of various oxygen-containing species. The changes of W 4f binding energy in the two H₃PW₁₂O₄₀/C₃N₄ NTs samples compared with a pure H₃PW₁₂O₄₀ sample can further confirm the existence of covalent C-O-W bonds at the interface of H₃PW₁₂O₄₀ and C₃N₄ NTs (Fig. 6d).

3.2.3. Optical and electronic properties

The light absorption property of bulk g-C₃N₄, H₃PW₁₂O₄₀ precursor, C₃N₄ NTs, and the representative H₃PW₁₂O₄₀/C₃N₄ NTs (3:10) was analyzed via UV-vis/DRS, and the result is shown in Fig. 7. The bulk g-C₃N₄ exhibits typical semiconductor absorption in the region ranging from 200 nm to 460 nm. This absorption originates from the charge transfer response of bulk g-C₃N₄ from

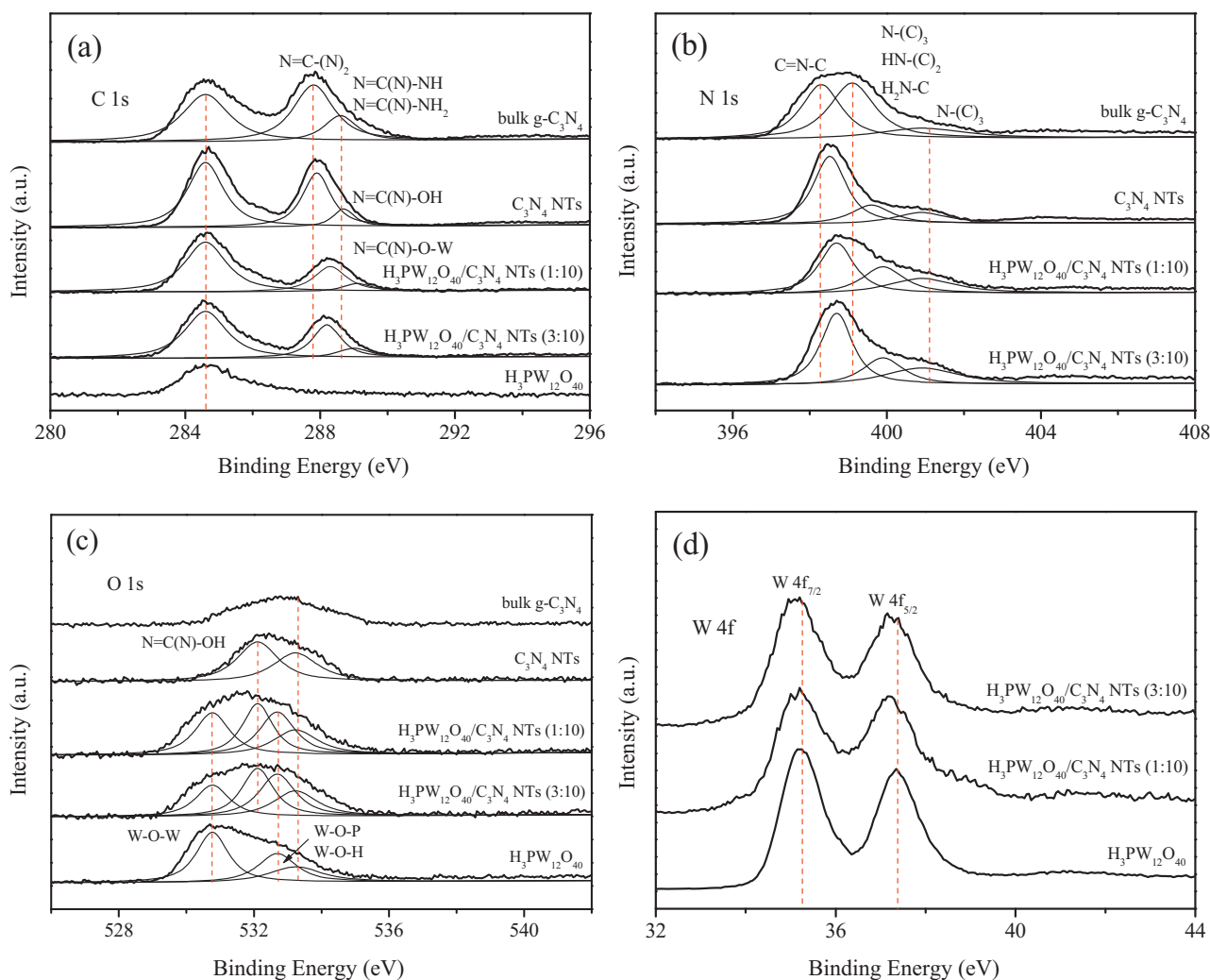


Fig. 6. High-resolution XPS of bulk g-C₃N₄, C₃N₄ NTs, H₃PW₁₂O₄₀ precursor, and H₃PW₁₂O₄₀/C₃N₄ NTs in the C 1s (a), N 1s (b), O 1s (c), and W 4f (d) binding energy regions.

the valence band populated by N 2p orbits to the conduction band formed with C 2p orbits. The estimated band gap energy of bulk g-C₃N₄ is about 2.7 eV, which is consistent with the results reported in the literature [45]. The light harvesting capability of C₃N₄ NTs is better enhanced in the region ranging from 200 nm to 400 nm compared with that of bulk g-C₃N₄ because a tubular

nanostructure is more beneficial than a bulk structure with regard to multiple reflections of incident light [46]. Light absorption of H₃PW₁₂O₄₀ precursor in the region ranging from 200 nm to 415 nm is attributed to charge transfer response from O 2p to W 5d orbit at W=O and W–O–W bonds, respectively. The estimated band gap energy of H₃PW₁₂O₄₀ is about 3.0 eV, which is also consistent with result in the literature [47]. The absorption edge of the H₃PW₁₂O₄₀/C₃N₄ NTs (3:10) sample red-shifts slightly compared with that of C₃N₄ NTs as a result of the doping level generated between C 2p and N 2p orbits, which reduced band gap energy. The estimated H₃PW₁₂O₄₀/C₃N₄ NTs (3:10) band gap energy is approximately 2.65 eV. The light-harvesting capability of H₃PW₁₂O₄₀/C₃N₄ NTs (3:10) increases in the region ranging from 200 nm to 400 nm compared with that of C₃N₄ NTs because of the intense light absorption by H₃PW₁₂O₄₀ clusters. Decreased band gap energy and enhanced light harvesting ability are both advantageous in enhancing the light utilization efficiency of H₃PW₁₂O₄₀/C₃N₄ NTs. Fig. 7 also shows that the absorption peak related to either H₃PW₁₂O₄₀ or C₃N₄ NTs is hardly detected in the H₃PW₁₂O₄₀/C₃N₄ NTs (3:10) sample, indicating that H₃PW₁₂O₄₀ homogeneously distributed throughout the whole hybrid material.

The optical and electronic properties of H₃PW₁₂O₄₀/C₃N₄ NTs are investigated further through PL measurement. The PL spectrum of the material originates from the radiative recombination of free e[−]–h⁺ carriers and helps clarify the migration and recombination processes of photogenerated carriers in a semiconductor

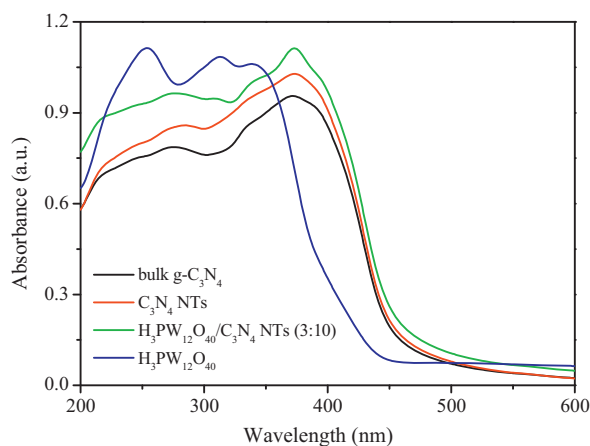


Fig. 7. UV-vis/DRS of bulk g-C₃N₄, C₃N₄ NTs, H₃PW₁₂O₄₀ precursor, and H₃PW₁₂O₄₀/C₃N₄ NTs (3:10).

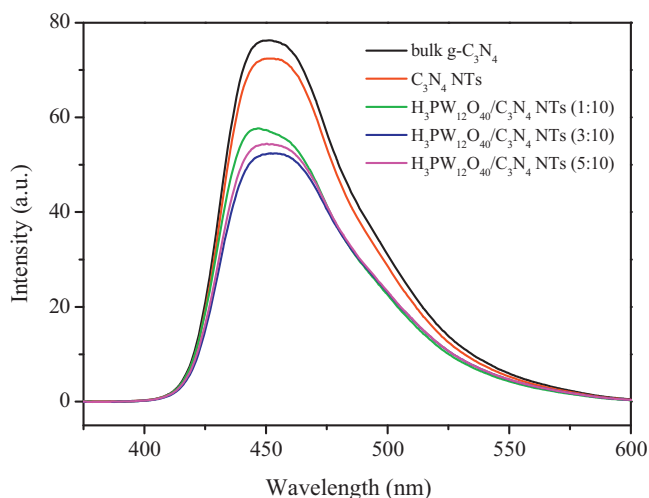


Fig. 8. PL spectra of bulk g-C₃N₄, C₃N₄ NTs, and H₃PW₁₂O₄₀/C₃N₄ NTs.

photocatalyst [48,49]. Bulk g-C₃N₄ exhibits luminescence in a broad range (410–550 nm) and is centered at ca. 450 nm under room temperature with an excitation wavelength of 330 nm, as shown in Fig. 8. This finding suggests that photoinduced e[−]–h⁺ are generated and recombined within the g-C₃N₄ semiconductor. The PL intensity of the C₃N₄ NTs sample decreases compared with that of bulk g-C₃N₄, suggesting the deceleration of e[−]–h⁺ recombination rate in the C₃N₄ NTs. This property originates from the efficient photoexcited carrier transfer in the C₃N₄ NTs as a result of their unique tubular nanostructure. The PL intensity of H₃PW₁₂O₄₀/C₃N₄ NTs gradually decrease compared with that of C₃N₄ NTs when the mass ratio of H₃PW₁₂O₄₀ to g-C₃N₄ increases from 1:10 to 3:10. This gradual decrease in PL intensity is attributed to the electron capture capability of Keggin units, which decelerate the e[−]–h⁺ recombination rate. However, the PL intensity increases slightly when the mass ratio of H₃PW₁₂O₄₀ to g-C₃N₄ is increased further to 5:10. This result suggests that the H₃PW₁₂O₄₀/C₃N₄ NTs under high H₃PW₁₂O₄₀ loads exhibit weak photoexcited carrier transfer capability because excessive H₃PW₁₂O₄₀ may form new e[−]–h⁺ recombination centers.

Photoinduced e[−]–h⁺ generation, separation, migration, and capture by reactive species is considered a basic process in semiconductor photocatalyst operation. Photoelectrochemistry tests are powerful tools to monitor these complicated processes. Sharp increases in photocurrent responses can be observed in all tested working electrodes once pulse Xe lamp irradiation is activated, as displayed by the photocurrent–time (*I*–*t*) curves shown in Fig. 9. The generated photocurrents are reproducible and stable during five intermittent on–off irradiation cycles. The prompt increase in photocurrent response from the light–off to the light–on state is mainly ascribed to the quick separation and transportation of photogenerated electrons on the surfaces of working electrodes. C₃N₄ NTs exhibit higher photocurrent response than bulk g-C₃N₄ under similar conditions and the photocurrent response of H₃PW₁₂O₄₀/C₃N₄ NTs is higher than that of C₃N₄ NTs. The photocurrent responses of H₃PW₁₂O₄₀/C₃N₄ NTs gradually increase when the mass ratio of H₃PW₁₂O₄₀ to g-C₃N₄ increases from 1:10 to 3:10. However, the photocurrent declines when the mass ratio is further increased to 5:10. The photoelectrochemical experiment results are consistent with the PL measurements described above, indicating that tubular nanostructure and H₃PW₁₂O₄₀ doping can effectively slow down the photogenerated e[−]–h⁺ recombination rate. The declined photocurrent responses of H₃PW₁₂O₄₀/C₃N₄ NTs (5:10) are attributed to new photogenerated e[−]–h⁺ recombination

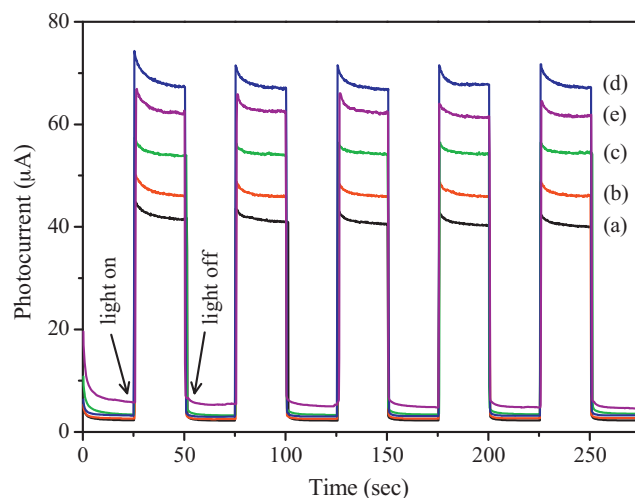


Fig. 9. Photocurrent responses of bulk g-C₃N₄ (a), C₃N₄ NTs (b), H₃PW₁₂O₄₀/C₃N₄ NTs (1:10) (c), H₃PW₁₂O₄₀/C₃N₄ NTs (3:10) (d), and H₃PW₁₂O₄₀/C₃N₄ NTs (5:10) (e) electrodes under Xe lamp irradiation.

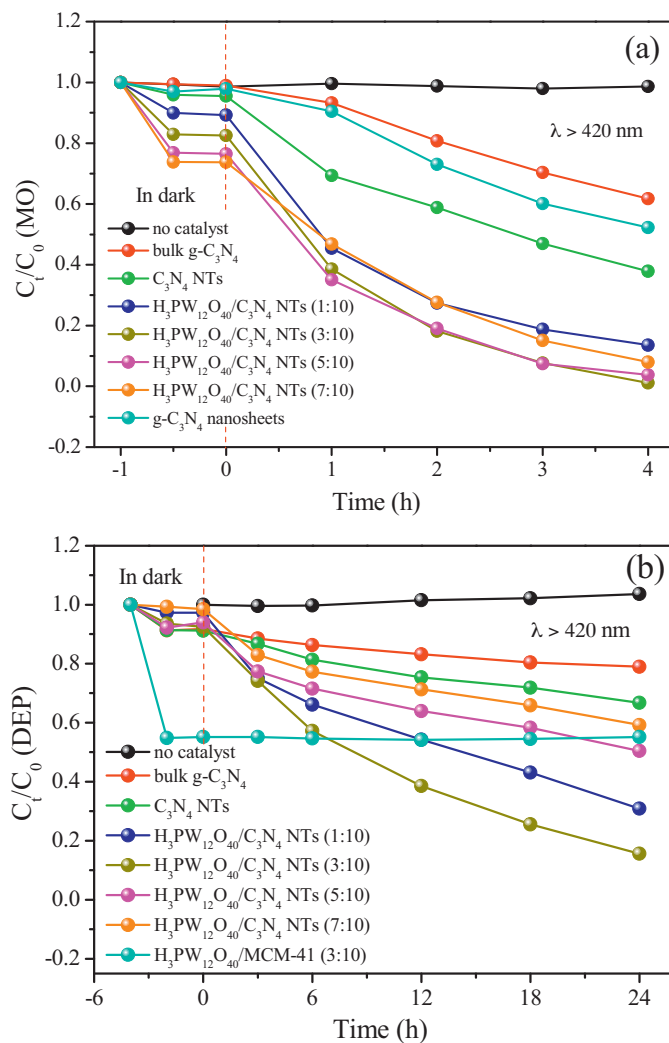


Fig. 10. Adsorption properties and photocatalytic activities of as-prepared photocatalysts toward aqueous MO (a) and DEP (b) removal under visible-light irradiation. Excitation wavelength $\lambda > 420$ nm; catalyst amount 200 mg; initial concentration $C_0 = 10$ mg L^{−1}; volume 100 mL.

centers induced as a result of the increased size and aggregation of Keggin units. These new recombination centers prohibit further photogenerated $e^- - h^+$ fabrication.

3.3. Photocatalytic tests

3.3.1. Adsorption and photocatalytic degradation of aqueous MO and DEP

Photocatalytic tests were conducted in an aqueous solution containing oxygen molecules from dissolved air. Visible-light irradiation was provided by a Xe lamp, and UV irradiation was eliminated using a 420 nm cut filter. The results of the direct photodegradation experiment indicate that changes in MO and DEP concentrations in the reaction system are negligible under visible-light irradiation for 4 and 24 h, respectively, as shown in Fig. 10. The adsorption test results show that the adsorption–desorption equilibrium was reached prior to Xe lamp irradiation. Bulk $g\text{-C}_3\text{N}_4$, $g\text{-C}_3\text{N}_4$ nanosheets, and C_3N_4 NTs display similar adsorption capacities to MO molecules based on the adsorption experiment presented in Fig. 10a. However, the adsorption capacity of $\text{H}_3\text{PW}_{12}\text{O}_{40}/\text{C}_3\text{N}_4$ NTs to MO molecules is gradually enhanced when the mass ratio of $\text{H}_3\text{PW}_{12}\text{O}_{40}$ to $g\text{-C}_3\text{N}_4$ increases from 1:10 to 7:10 because of the existence of chemical adsorption between Keggin unit and MO molecules. Except $\text{H}_3\text{PW}_{12}\text{O}_{40}/\text{MCM-41}$ (3:10) sample, all the tested materials exhibit a similar adsorption capacity to DEP molecules, as shown in Fig. 10b. $\text{H}_3\text{PW}_{12}\text{O}_{40}/\text{MCM-41}$ (3:10) has the highest adsorption capacity among seven tested materials, indicating that the adsorption capacities of the tested materials to DEP molecules are related to surface area. The DEP molecules adsorption by tested materials is mainly physical. The high adsorption capacity of $\text{H}_3\text{PW}_{12}\text{O}_{40}/\text{MCM-41}$ (3:10) to DEP molecules originates from its large surface area (ca. $850\text{ m}^2\text{ g}^{-1}$). The photocatalytic tests obtain similar results with respect to both MO and DEP degradation. The photocatalytic activity of C_3N_4 NTs is higher than that of bulk $g\text{-C}_3\text{N}_4$, and the photocatalytic activity of $\text{H}_3\text{PW}_{12}\text{O}_{40}/\text{C}_3\text{N}_4$ NTs is higher than that of C_3N_4 NTs. The photocatalytic activities of $\text{H}_3\text{PW}_{12}\text{O}_{40}/\text{C}_3\text{N}_4$ NTs increase monotonously when the mass ratios of $\text{H}_3\text{PW}_{12}\text{O}_{40}$ to $g\text{-C}_3\text{N}_4$ increase from 1:10 to 3:10. However, the photocatalytic activities decrease gradually when the mass ratios further increase to 5:10 and 7:10, respectively. $\text{H}_3\text{PW}_{12}\text{O}_{40}/\text{C}_3\text{N}_4$ NTs (3:10) sample is the most photoactive among all of the tested materials. MO and DEP are degraded completely after 4 and 24 h visible-light irradiation, respectively. The photocatalytic activity of $g\text{-C}_3\text{N}_4$ nanosheets is higher than bulk $g\text{-C}_3\text{N}_4$ but lower than C_3N_4 NTs to the MO degradation. This result suggests that nanostructure design is an effective strategy to improve the photocatalytic activity of bulk $g\text{-C}_3\text{N}_4$, but tubular nanostructure is more favorable to the diffusion and transmission of reaction molecules in the catalytic reaction process. Similar results have been reported by other groups [50]. In the case of $\text{H}_3\text{PW}_{12}\text{O}_{40}/\text{MCM-41}$ (3:10) sample, changes in DEP concentration are hardly observed during visible-light irradiation, implying that the $\text{H}_3\text{PW}_{12}\text{O}_{40}$ precursor cannot be photoactivated by current visible-light irradiation.

3.3.2. Mineralization and degradation mechanism of aqueous MO and DEP

The mineralization of aqueous MO and DEP was evaluated by monitoring the changes in total organic carbon (TOC) in the reaction system. The result is shown in Fig. 11. $\text{H}_3\text{PW}_{12}\text{O}_{40}/\text{C}_3\text{N}_4$ NTs (3:10) were selected as the representative photocatalysts. TOC of MO and DEP are degraded by 38.2% and 24.5%, respectively, after exposure to visible-light irradiation for 48 h, indicating that the produced organic intermediates continue to decompose into inorganic species. DEP mineralization rate is slower than that of MO under

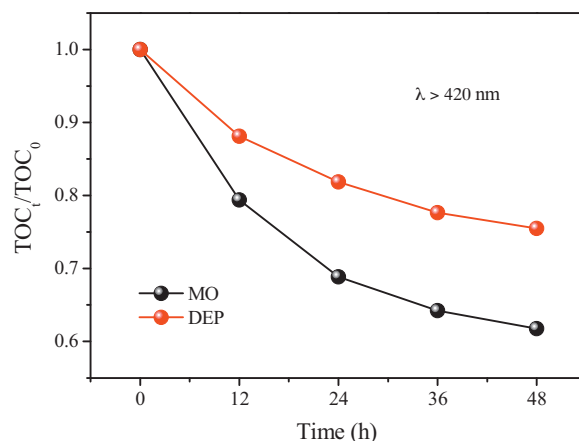
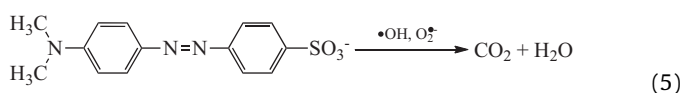
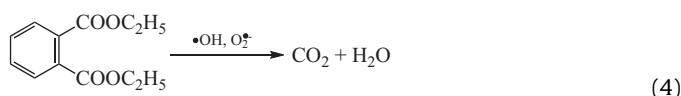
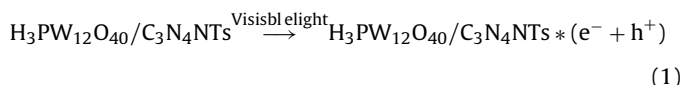


Fig. 11. Evolution of TOC during the course of photocatalytic degradation of aqueous MO and DEP over $\text{H}_3\text{PW}_{12}\text{O}_{40}/\text{C}_3\text{N}_4$ NTs (3:10) photocatalyst. Excitation wavelength $\lambda > 420\text{ nm}$; catalyst amount 200 mg; initial concentration $C_0 = 10\text{ mg L}^{-1}$; volume 100 mL.

similar conditions because of the stable chemical structure of the DEP molecule.

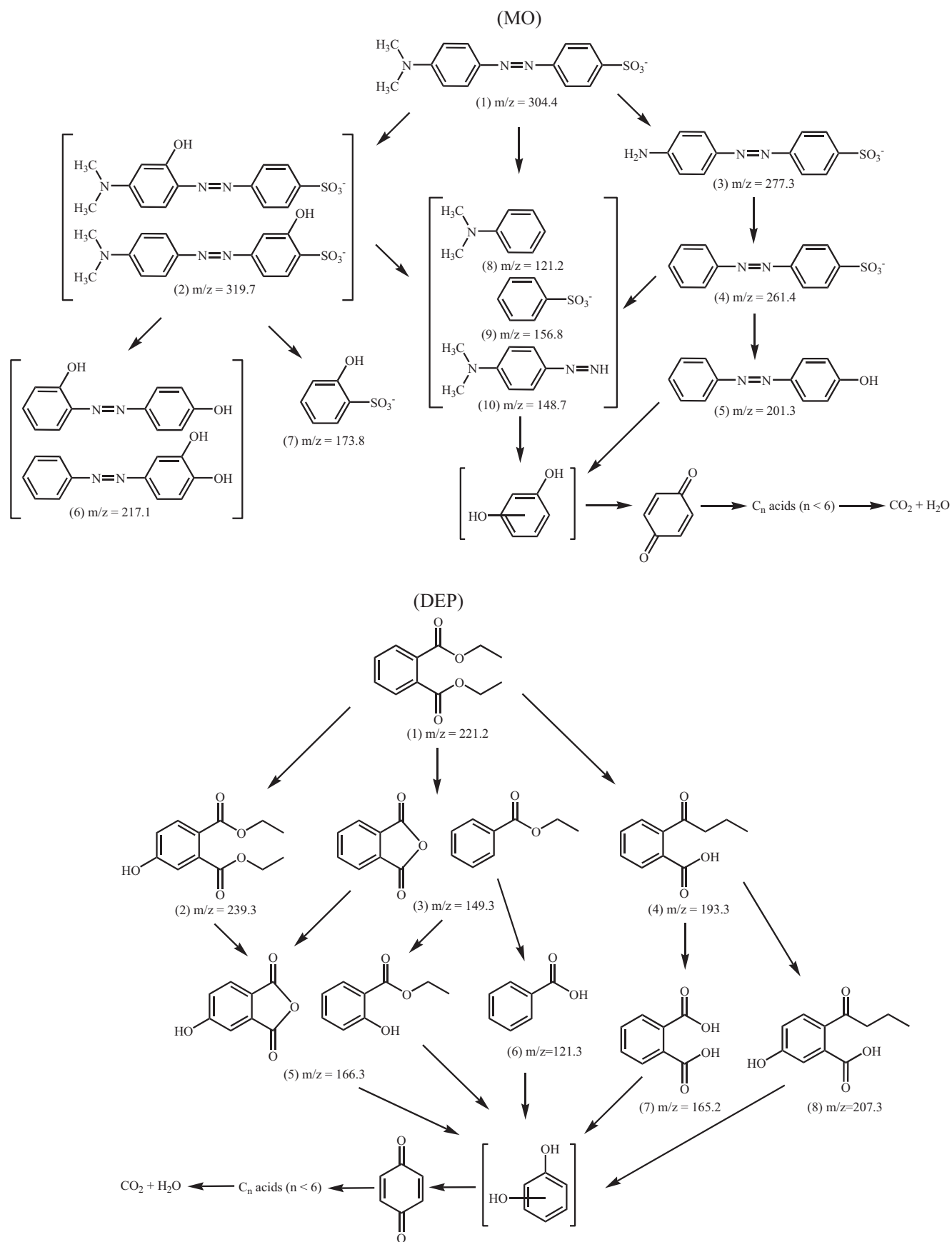
Aqueous MO and DEP degradation may be clarified by the mechanistic explanation regarding semiconductor photocatalytic oxidative degradation of POPs in an aqueous system using Eqs. (1)–(5):



High-performance liquid chromatography tandem mass spectrometry (HPLC/MS) results show that 10 and 8 intermediates were generated during MO and DEP degradation, respectively. The proposed aqueous MO and DEP degradation pathway using $\text{H}_3\text{PW}_{12}\text{O}_{40}/\text{C}_3\text{N}_4$ NTs in visible-light irradiation according to the results of HPLC/MS analysis is shown in Scheme 2.

3.3.3. Recyclability of $\text{H}_3\text{PW}_{12}\text{O}_{40}/\text{C}_3\text{N}_4$ NTs hybrid materials

DEP was selected as a target pollutant and $\text{H}_3\text{PW}_{12}\text{O}_{40}/\text{C}_3\text{N}_4$ NTs (3:10) as a representative photocatalyst to evaluate the stability of the hybrid materials in the current photocatalytic reaction system. The DEP degradation reaction mentioned above was repeated four times. The catalyst was recovered by centrifugation and filtration after the first catalytic run, and was dried at 60°C for 12 h. The recovered catalyst was used in the second and third catalytic runs under similar experimental conditions and regeneration methods. The results indicate that photocatalytic activity is gradually lost after the second and third catalytic runs (Fig. 12). However, the $\text{H}_3\text{PW}_{12}\text{O}_{40}$ leaching is not detected when the catalyst-free reaction solution was analyzed by ICP-AES, implying that the loss of catalytic reactivity is a consequence of the adsorption of DEP molecules and/or organic intermediate products by $\text{H}_3\text{PW}_{12}\text{O}_{40}/\text{C}_3\text{N}_4$ NTs (3:10) rather than of $\text{H}_3\text{PW}_{12}\text{O}_{40}$ leaching. Therefore, the reused catalyst was calcined at 300°C for 1 h



Scheme 2. Proposed degradation pathway of aqueous MO and DEP by $H_3PW_{12}O_{40}/C_3N_4$ NTs under visible-light irradiation.

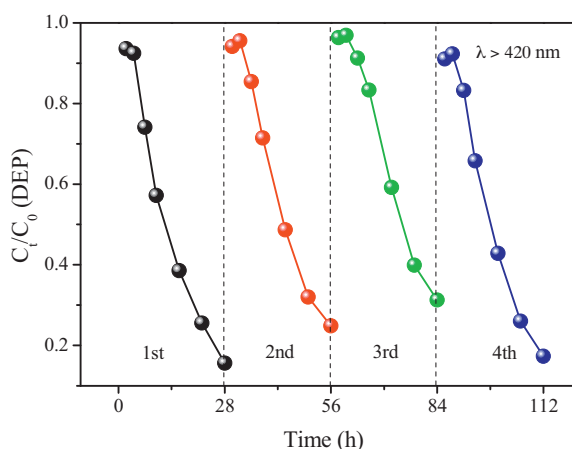


Fig. 12. Recycling experiments of photocatalytic degradation of aqueous DEP over $\text{H}_3\text{PW}_{12}\text{O}_{40}/\text{C}_3\text{N}_4$ NTs (3:10) photocatalyst. Excitation wavelength $\lambda > 420$ nm; catalyst amount 200 mg; initial concentration $C_0 = 10 \text{ mg L}^{-1}$; volume 100 mL.

to remove the adsorbed organic species. As expected, the catalytic reactivity was almost restored in the fourth run. Through analysis of results of TEM and FESEM images and corresponding W elemental mappings of the used $\text{H}_3\text{PW}_{12}\text{O}_{40}/\text{C}_3\text{N}_4$ NTs (3:10) it is found that the tubular nanostructure remains intact and $\text{H}_3\text{PW}_{12}\text{O}_{40}$ remains homogeneously distribute throughout the hybrid materials after four photocatalytic runs (Fig. S2).

3.3.4. Discussion to photocatalytic results

The excellent photocatalytic activity of the $\text{H}_3\text{PW}_{12}\text{O}_{40}/\text{C}_3\text{N}_4$ NTs prepared through one-step hydrothermal treatment is primarily attributed to the following three reasons.

First, the incorporation of the Keggin unit into C_3N_4 NTs can enhance photocatalytic quantum efficiency because of the strong electron acceptability of the Keggin unit. The synergistic photocatalytic effect of the Keggin unit on C_3N_4 NTs retards the recombination of e^- – h^+ pairs because photogenerated electrons are trapped in the unoccupied W 5d states of the Keggin unit. Therefore, the photocatalytic activity of $\text{H}_3\text{PW}_{12}\text{O}_{40}/\text{C}_3\text{N}_4$ NTs is gradually enhanced when the mass ratio of $\text{H}_3\text{PW}_{12}\text{O}_{40}$ to g- C_3N_4 increases from 1:10 to 3:10. However, the photocatalytic activity of $\text{H}_3\text{PW}_{12}\text{O}_{40}/\text{C}_3\text{N}_4$ NTs gradually declines when the mass ratio is increased further to 5:10 and 7:10. This result suggests that exorbitant $\text{H}_3\text{PW}_{12}\text{O}_{40}$ loads may enrich tungsten atoms on the catalyst surface, creating new e^- – h^+ pair recombination centers with decreased photocatalytic activity.

Second, tubular nanostructure formation has an important function in enhancing the photocatalytic activity of bulk g- C_3N_4 . Fabrication of C_3N_4 NTs can increase the number of active sites, as well as accessibility to the active sites. A tubular nanostructure can ensure the target pollutant degradation reaction performed in the C_3N_4 NTs and thereby lower the mass transfer limit. C_3N_4 NTs can improve catalytic reactivity by facilitating accessibility to active sites. Guest species are efficiently transported throughout the tubular photocatalyst, and the reaction is not limited to the catalyst surface. A tubular nanostructure can also reduce the probability of e^- – h^+ pair recombination by improving electron transfer capability, thereby prolonging charge lifespan and transferring photogenerated charges to the reactants. Thus, the photocatalytic activity of C_3N_4 NTs is higher than that of bulk g- C_3N_4 .

Third, the high light-utilization efficiency of $\text{H}_3\text{PW}_{12}\text{O}_{40}/\text{C}_3\text{N}_4$ NTs has a positive effect on photocatalytic activity because it is favorable in the increased production of photogenerated e^- – h^+ under similar visible-light irradiation.

4. Conclusions

A series of $\text{H}_3\text{PW}_{12}\text{O}_{40}/\text{C}_3\text{N}_4$ NTs is successfully fabricated using one-step hydrothermal treatment strategy. Tubular nanostructures are formed through a nanosheet roll-up mechanism. The as-prepared $\text{H}_3\text{PW}_{12}\text{O}_{40}/\text{C}_3\text{N}_4$ NTs with suitable $\text{H}_3\text{PW}_{12}\text{O}_{40}$ loading exhibit considerably high photocatalytic activity and stability with respect to MO and DEP degradation under visible-light irradiation. The high photocatalytic activity is attributed to their unique tubular nanostructure, enhanced quantum efficiency, and high light-utilization efficiency. Their high catalytic stability is attributed to the strong chemical interaction between the Keggin unit and the C_3N_4 NTs. The as-prepared hybrid materials can maintain similar levels of activity after four catalytic cycles using a suitable regeneration method. The $\text{H}_3\text{PW}_{12}\text{O}_{40}/\text{C}_3\text{N}_4$ NTs hybrid materials are expected to be widely used as a visible-light photocatalyst in aqueous POPs degradation. They may also be broadly applied in other areas, such as hydrogen production from water-splitting, oxidation reaction and NO decomposition.

Acknowledgements

This work was financially supported by the National Natural Science Foundation of China (51238002, 51272099, 51208248, 51278092, 21366024, 21165013); Youth Science Foundation of Jiangxi Province, China (20114BAB213015); Youth Science Foundation of Jiangxi Provincial Department of Education, China (GJJ12456).

Appendix A. Supplementary data

Supplementary data associated with this article can be found, in the online version, at <http://dx.doi.org/10.1016/j.apcatb.2014.03.010>.

References

- [1] M. Hu, Y. Wang, Z. Xiong, D. Bi, Y. Zhang, Y. Xu, *Environ. Sci. Technol.* 46 (2012) 9005–9011.
- [2] B. Tian, T. Wang, R. Dong, S. Bao, F. Yang, J. Zhang, *Appl. Catal. B: Environ.* 147 (2014) 22–28.
- [3] S. Yu, H.J. Yun, Y.H. Kim, J. Yi, *Appl. Catal. B: Environ.* 144 (2014) 893–899.
- [4] X. Wang, K. Maeda, A. Thomas, K. Takanabe, G. Xin, J.M. Carlsson, K. Domen, M. Antonietti, *Nat. Mater.* 8 (2009) 76–80.
- [5] C. Han, L. Ge, C. Chen, Y. Li, X. Xiao, Y. Zhang, L. Guo, *Appl. Catal. B: Environ.* 147 (2014) 546–553.
- [6] S. Wang, D. Li, C. Sun, S. Yang, Y. Guan, H. He, *Appl. Catal. B: Environ.* 144 (2014) 885–892.
- [7] S. Zhang, Y. Yang, Y. Guo, W. Guo, M. Wang, Y. Guo, M. Huo, *J. Hazard. Mater.* 261 (2013) 235–245.
- [8] Y.S. Jun, J. Park, S.U. Lee, A. Thomas, W.H. Hong, G.D. Stucky, *Angew. Chem. Int. Ed.* 125 (2013) 11289–11293.
- [9] P. Niu, L. Zhang, G. Liu, H. Cheng, *Adv. Funct. Mater.* 22 (2012) 4763–4770.
- [10] Z. Lin, X. Wang, *Angew. Chem. Int. Ed.* 125 (2013) 1779–1782.
- [11] S. Yang, Y. Gong, J. Zhang, L. Zhan, L. Ma, Z. Fang, R. Vajtai, X. Wang, P.M. Ajayan, *Adv. Mater.* 25 (2013) 2452–2456.
- [12] A. Du, S. Sanvito, Z. Li, D. Wang, Y. Jiao, T. Liao, Q. Sun, Y.H. Ng, Z. Zhu, R. Amal, S.C. Smith, *J. Am. Chem. Soc.* 134 (2012) 4393–4397.
- [13] B.K. Vijayan, N.M. Dimitrijevic, D. Finkelstein-Shapiro, J. Wu, K.A. Gray, *ACS Catal.* 2 (2012) 223–229.
- [14] B.K. Vijayan, N.M. Dimitrijevic, J. Wu, K.A. Gray, *J. Phys. Chem. C* 114 (2010) 21262–21269.
- [15] D. Wang, L. Liu, F. Zhang, K. Tao, E. Pippel, K. Domen, *Nano Lett.* 11 (2011) 3649–3655.
- [16] K.C. Huang, S.H. Chien, *Appl. Catal. B: Environ.* 140–141 (2013) 283–288.
- [17] J. Gao, Y. Zhou, Z. Li, S. Yan, N. Wang, Z. Zou, *Nanoscale* 4 (2012) 3687–3692.
- [18] S.W. Bian, Z. Ma, W.G. Song, *J. Phys. Chem. C* 113 (2009) 8668–8672.
- [19] W.H. Shin, S.H. Yang, Y.J. Choi, H.M. Jung, C.O. Song, J.K. Kang, *J. Mater. Chem.* 19 (2009) 4505–4509.
- [20] P. Liu, H. Zhang, H. Liu, Y. Wang, X. Yao, G. Zhu, S. Zhang, H. Zhao, *J. Am. Chem. Soc.* 133 (2011) 19032–19035.
- [21] R.D. White, D.V. Bavykin, F.C. Walsh, *J. Mater. Chem. A* 1 (2013) 548–556.
- [22] A. Nakahira, T. Kubo, C. Numako, *Inorg. Chem.* 49 (2010) 5845–5852.
- [23] L. Ge, C. Han, J. Liu, Y. Li, *Appl. Catal. A: Gen.* 409–410 (2011) 215–222.

- [24] K. Ghosh, M. Kumar, H. Wang, T. Maruyama, Y. Ando, *J. Phys. Chem. C* 114 (2010) 5107–5112.
- [25] L. Ge, F. Zuo, J. Liu, Q. Ma, C. Wang, D. Sun, L. Bartels, P. Feng, *J. Phys. Chem. C* 116 (2012) 13708–13714.
- [26] N. Lu, Y. Zhao, H. Liu, Y. Guo, X. Yuan, H. Xu, H. Peng, H. Qin, *J. Hazard. Mater.* 199–200 (2012) 1–8.
- [27] S. Zhang, L. Chen, H. Liu, W. Guo, Y. Yang, Y. Guo, M. Huo, *Chem. Eng. J.* 200–202 (2012) 300–309.
- [28] K. Li, Y. Guo, F. Ma, H. Li, L. Chen, Y. Guo, *Catal. Commun.* 11 (2010) 839–843.
- [29] K. Li, X. Yang, Y. Guo, F. Ma, H. Li, L. Chen, Y. Guo, *Appl. Catal. B: Environ.* 99 (2010) 364–375.
- [30] S. Na, Y.G. Ahn, M. Cui, J. Khim, *J. Environ. Manage.* 101 (2012) 104–110.
- [31] H. Wang, D.Z. Sun, Z.Y. Bian, *J. Hazard. Mater.* 180 (2010) 710–715.
- [32] B. Xu, N.Y. Gao, X.F. Sun, S.J. Xia, M. Rui, M.O. Simonnot, C. Causserand, J.F. Zhao, *J. Hazard. Mater.* 139 (2007) 132–139.
- [33] H. Maruyama, H. Seki, Y. Matsukawa, A. Suzuki, N. Inoue, *Ind. Eng. Chem. Res.* 45 (2006) 6383–6386.
- [34] Y. Kang, W. Den, H. Bai, *Ind. Eng. Chem. Res.* 45 (2006) 1331–1336.
- [35] Y. Guo, K. Li, X. Yu, J.H. Clark, *Appl. Catal. B: Environ.* 81 (2008) 182–191.
- [36] M.D. Hernández-Alonso, S. García-Rodríguez, B. Sánchez, J.M. Coronado, *Nanoscale* 3 (2011) 2233–2240.
- [37] R.D. White, D.V. Bavykin, F.C. Walsh, *J. Mater. Chem. A* 1 (2013) 548–556.
- [38] D.V. Bavykin, V.N. Parmon, A.A. Lapkin, F.C. Walsh, *J. Mater. Chem.* 14 (2004) 3370–3377.
- [39] Y. Yang, Y. Guo, F. Liu, X. Yuan, Y. Guo, S. Zhang, W. Guo, M. Huo, *Appl. Catal. B: Environ.* 142–143 (2013) 828–837.
- [40] P. Niu, G. Liu, H.M. Cheng, *J. Phys. Chem. C* 116 (2012) 11013–11018.
- [41] X.H. Li, X. Wang, M. Antonietti, *ACS Catal.* 2 (2012) 2082–2086.
- [42] K. Li, J. Hu, W. Li, F. Ma, L. Xu, Y. Guo, *J. Mater. Chem.* 19 (2009) 8628–8638.
- [43] J. Zhang, M. Zhang, G. Zhang, X. Wang, *ACS Catal.* 2 (2012) 940–948.
- [44] S.C. Yan, Z.S. Li, Z.G. Zou, *Langmuir* 26 (2010) 3894–3901.
- [45] J. Zhang, X. Chen, K. Takanabe, K. Maeda, K. Domen, J.D. Epping, X. Fu, M. Antonietti, X. Wang, *Angew. Chem. Int. Ed.* 49 (2010) 441–444.
- [46] J. Zhang, F. Guo, X. Wang, *Adv. Funct. Mater.* 23 (2013) 3008–3014.
- [47] Y. Guo, C. Hu, *J. Mol. Catal. A: Chem.* 262 (2007) 136–148.
- [48] X. Bai, R. Zong, C. Li, D. Liu, Y. Liu, Y. Zhu, *Appl. Catal. B: Environ.* 147 (2014) 82–91.
- [49] S.W. Cao, X.F. Liu, Y.P. Yuan, Z.Y. Zhang, Y.S. Liao, J. Fang, S.C.J. Loo, T.C. Sum, C. Xue, *Appl. Catal. B: Environ.* 147 (2014) 940–946.
- [50] Z. Chang, J. Liu, J. Liu, X. Sun, *J. Mater. Chem.* 21 (2011) 277–282.